processes

MDPI

Article

Effects of Superheated Surface on the Deposition Behavior of Na_2SO_4 in Supercritical Water

Qiao Zhu [1], Zhe Li [1], Yafei Song [1], Yujun Tong [2], Tao Yang [2] and Zhenmin Cheng [1,*]

[1] State Key Laboratory of Chemical Engineering, School of Chemical Engineering, East China University of Science and Technology, Shanghai 200237, China; y30200072@mail.ecust.edu.cn (Q.Z.); y20200004@mail.ecust.edu.cn (Z.L.); y30190934@mail.ecust.edu.cn (Y.S.)

[2] Dalian Research Institute of Petroleum and Petrochemicals, SINOPEC, Dalian 116000, China; tongyujun.fshy@sinopec.com (Y.T.); yt.fshy@sinopec.com (T.Y.)

* Correspondence: zmcheng@ecust.edu.cn

Abstract: The reduced solubility of inorganic salts in supercritical water has a significant impact on the stable operation of desalination facilities as it may lead to surface fouling due to salt deposition. In this study, the solubility of Na_2SO_4 was experimentally determined to be 0.04–15.34 mmol/kg water at 23–25 MPa and 390–420 °C. To investigate the precipitation behavior of Na_2SO_4 in supercritical water, a reactor with a heating bar was designed and the deposition effect of salt on the superheated surface in an autoclave was tested at a temperature of 390 °C and a pressure of 23 MPa. Then, the deposition mechanism of salt in the autoclave was analyzed and the temperature field in the reactor was simulated using CFD commercial software. The experimental results showed that Na_2SO_4 was present on both the heating rod and the bottom of the autoclave with a loose salt layer. The simulation results indicated that the temperature near the heating rod was significantly higher than the bulk fluid temperature and it provided the temperature condition where the inorganic salt preferentially nucleated and precipitated. Nickel foam was chosen as the porous media carrier to investigate the selective precipitation of salt on different superheated surfaces. The results showed that nickel foam could collect a large amount of salt on the heating rod and change the state of the compact salt layer on the kettle bottom wall, providing a technical choice for salt recovery under supercritical conditions.

Keywords: supercritical water; desalination; temperature effect; surface fouling

Citation: Zhu, Q.; Li, Z.; Song, Y.; Tong, Y.; Yang, T.; Cheng, Z. Effects of Superheated Surface on the Deposition Behavior of Na_2SO_4 in Supercritical Water. *Processes* **2023**, *11*, 1779. https://doi.org/10.3390/pr11061779

Academic Editor: Anna Wołowicz

Received: 27 April 2023
Revised: 5 June 2023
Accepted: 9 June 2023
Published: 11 June 2023

1. Introduction

Supercritical water is a fluid with a temperature greater than 374 °C and a pressure greater than 22.1 MPa [1]. It is characterized by a lower dielectric constant and density compared to those of water at a normal temperature and pressure. Specifically, the dielectric constant reduces from 78 (T = 25 °C, P = 0.1 MPa) to 6 (at critical point), whereas the density decreases from 997 kg/m^3 to 280 kg/m^3 [2]. Therefore, it has properties similar to non-polar solvents, resulting in the enhanced solubility of inorganic substances and reduced solubility of inorganic salts [3]. Due to its unique properties, supercritical water has found widespread applications in numerous processes, including supercritical water oxidation (SCWO) [4–7], supercritical water desalination (SCWD) [8–10], supercritical water gasification (SCWG) [11–13], supercritical hydrothermal synthesis (SHS) [14–16], etc. SCWO [4] is a homogeneous oxidation reaction that uses supercritical water as the reaction medium and oxygen and air as the oxidant to rapidly convert organic matter into harmless small molecules such as carbon dioxide and water. SCWD [8] exploits the non-polar characteristic of supercritical water to separate salts from wastewater and achieve zero liquid discharge of saline wastewater. SHS is commonly used for the synthesis of nanomaterials with the advantages of fast reaction rates and high product crystallinity. The process of SHS is particularly promising for the generation of high-performance

nanoparticles, which can be applied in various fields, such as enhancing the functionality of ion-selective electrodes [17].

Conventional methods for treating wastewater include membrane separation, biodegradation, chemical precipitation, and incineration [18–20]. However, these methods have limited application in treating high-salt organic wastewater. Membrane separation techniques, such as reverse osmosis and nanofiltration, are ineffective at removing organic matter from wastewater. Moreover, the membranes are susceptible to contamination during the treatment process, leading to reduced efficiency and service life and high costs [18]. High concentrations of salt in wastewater inhibit the survival of biological cells, thereby limiting the applicability of biological methods for large-scale wastewater treatment. Incineration methods are associated with secondary pollution [21]. In comparison to the traditional methods of treating high-salinity organic wastewater, SCWO technology has several advantages, such as a shorter reaction time, no secondary pollution, and environmental friendliness [21]. However, the solubility of inorganic salts is significantly reduced due to the decrease in the dielectric constant and density of supercritical water. For instance, the solubility of NaCl is only 1.44–87 mmol/kg at the temperature range of 380–400 °C and the pressure range of 18–23.5 MPa [22]. Similarly, the solubility of Na_2SO_4 decreases to 0.025–69.7 mmol/kg at a temperature range of 380–400 °C and a pressure of 25 MPa [23]. As a result, when the salt concentration in wastewater is high, inorganic salts precipitate and settle rapidly, forming a sedimentary layer that can block pipelines and interfere with heat transfer [24].

The application of SCWO has been limited due to issues of corrosion and blockage. These issues arise from the deposition of salts originating from the raw material solution or the oxidative decomposition of organic matter. To mitigate salt deposition during the SCWO process, the existing research has mainly focused on controlling salt concentration in the material to reduce deposition or on conducting one-step pretreatment to remove a portion of salt before entering the reactor [25]. Alternatively, reactor design can be employed to reduce salt deposition on the walls. Samuel et al. [8] designed a secondary separation process for the desalination of seawater, utilizing the non-polar properties of SCW to remove salt from brine in a separator.

In summary, reducing inorganic salt deposition in applications is typically achieved through reactor design and raw material pretreatment. However, methods to provide crystalline carriers have not been extensively studied. Dell'Orco et al. [26] added γ-Al_2O_3 spheres to provide the surface area for non-homogeneous precipitation when determining the solubility of $NaNO_3$ at 24.8–30 MPa and 450–525 °C, but the effect of γ-Al_2O_3 spheres on inorganic salts was not described. Moreover, few studies have explored the deposition characteristics of inorganic salts in the reactor, although it is suggested that superheated surfaces are more likely to be preferential sites for salt nucleation to occur [27]. Porous metals may provide a better medium to induce directed salt deposition due to their low density, large specific surface area, and good thermal conductivity.

In this study, a reactor with an in-built suspended heating rod was designed. Taking typical type II Na_2SO_4 salt as a representative, the deposition of salt in the autoclave was tested at the temperature of 390 °C at 23 MPa, and the induction of deposition of the inorganic salt by nickel foam was also tested. The effect of gravity and different heating walls on salt crystallization was comprehensively investigated. Additionally, temperature and velocity field distributions in the autoclave were obtained through CFD simulations to analyze the results of salt deposition.

2. Experiment

2.1. Chemicals

Sodium sulfate (analytically pure, ≥99%) was purchased from Shanghai Aladdin Biochemical Technology Co., Ltd. (Shanghai, China), and deionized water was purchased from Shanghai Huazhen Technology Co., Ltd. (Shanghai, China). The details of the chemical reagents are listed in Table 1. Considering the corrosion effect under supercritical

conditions, nickel foam was selected as the primary experimental material. In this study, two different sizes of nickel foam were used: 50 × 50 × 5 (mm^3), and 25 × 25 × 5 (mm^3), both with a porosity of 20 PPI (pores per inch).

Table 1. Chemical reagents used in this work.

Chemical Reagent	Source	Mass Fraction Purity	Purification Method	CAS No.
Sodium sulfate anhydrous	Aladdin (Shanghai Aladdin Biochemical Technology Co., Ltd., Shanghai, China)	AR, 99%	None	7757-82-6
deionized water	Shanghai Huazhen Technology Co., Ltd., Shanghai, China	Conductivity < 1.75 μS/cm	None	7732-18-5

2.2. Device Process

Figure 1 illustrates the process of the device, in which the autoclave is made of Inconel625 alloy to resist corrosion in the supercritical state. Figure 2 displays a diagram of the experimental setup. The prepared test material was placed at the bottom of the autoclave or fixed to the heating rod with nickel wire. A specific concentration of salt solution was prepared by dissolving a weighed amount of the sample salt in deionized water and pumping it into the preheater with a high-pressure pump (10–100 mL/min). After preheating to 200–300 °C, the solution entered the reactor, where the brine was heated to the supercritical temperature (390–450 °C) using an electric heating furnace. Under the supercritical condition, salt particles were precipitated from the supercritical water. The desalinated solution was filtered by a filter (SS10TF-MM-2, Swagelok, OH, USA), and cooled to ambient temperature by a condenser. The overall pressure of the plant was controlled at 23 MPa by the back pressure valve (R42LG-BBG-11-11-P, Amflo, Shanghai, China).

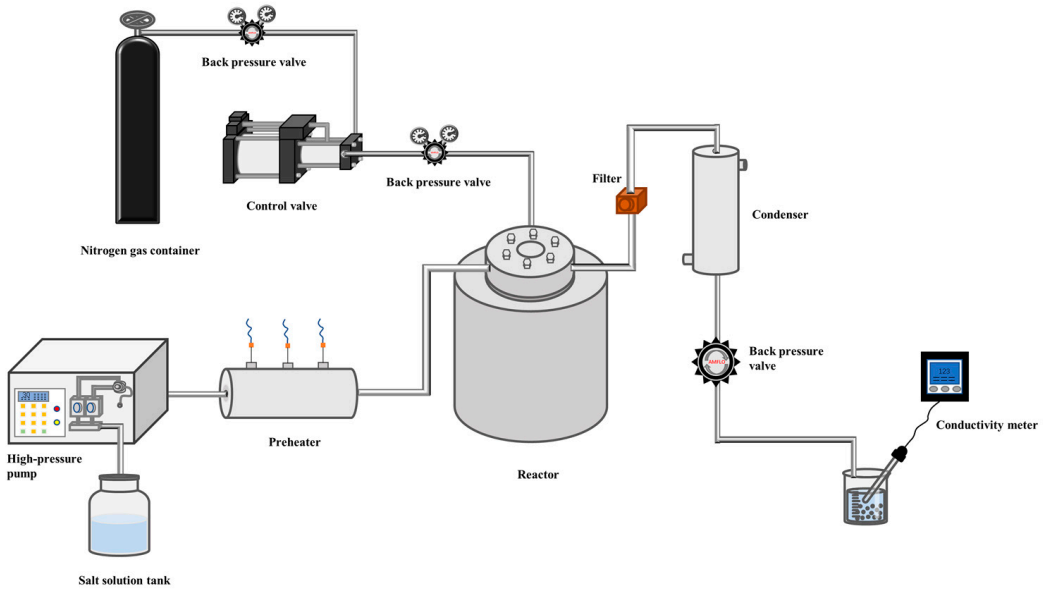

Figure 1. Flow chart of experimental device.

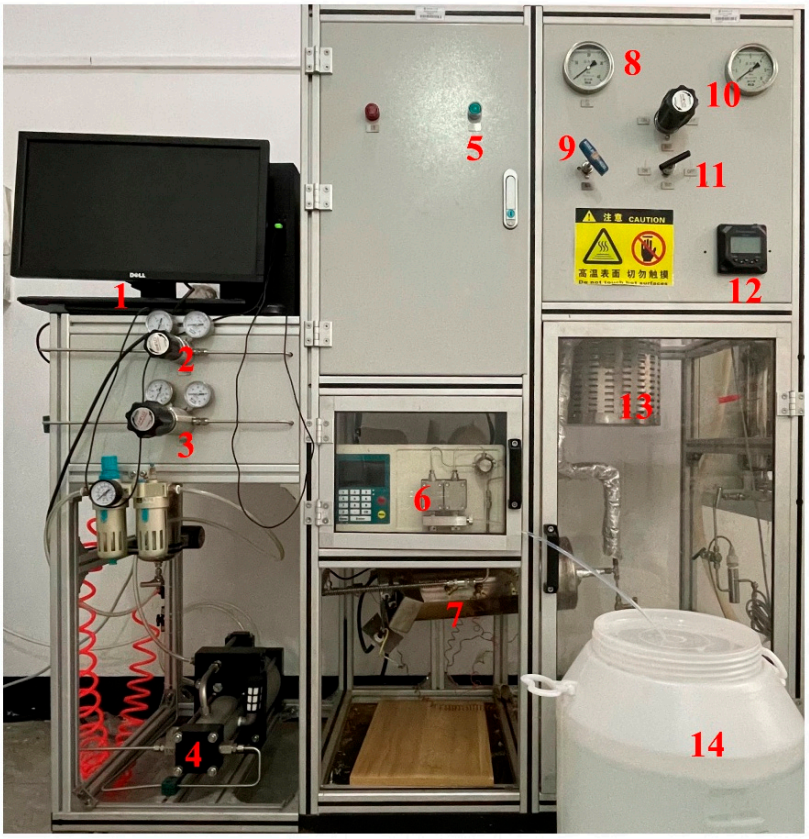

Figure 2. The experimental setup. 1—computer; 2,3—N_2 valve; 4—N_2 pump; 5—power supply; 6—liquid pump; 7—preheater; 8—pressure gauge; 9—valve; 10—back pressure valve; 11—bypass valve; 12—conductivity display; 13—autoclave; 14—tank.

The device operation and data measurements were controlled and acquired, respectively, by a computer. The relationship between the concentration of the inorganic salt solution and the conductivity was described by a linear equation, and the salt concentration in the solution was calculated from the conductivity values. The relationship between salt concentration and conductivity can be expressed as follows:

$$S = 0.0055 \cdot \sigma - 0.03826 \quad (1)$$

where S is the salt concentration in mmol/L; σ is the conductivity in μS/cm. The correlation coefficient $R^2 = 0.99932$ indicated that the relationship between concentration and conductivity was linear over the experimental concentration range. Figure 3 depicts the concentration of the Na_2SO_4 solution as a function of conductivity.

To investigate the impact of the superheated surface on salt deposition in the supercritical state, a heating rod (Figure 4) was designed for the autoclave, and the upper temperature of it could reach 600 °C. After the brine was injected for a certain time, when the conductivity value was maintained within a certain range, the solution was stopped. To avoid the residual gas in the kettle from redissolving the precipitated salt particles, a section of the nitrogen booster was placed at the front end of the reactor. An air compressor was used to pressurize nitrogen into the autoclave and bring out the residual water vapor. After depressurizing and waiting for the temperature to drop to a normal temperature, the carrier material was removed and the experimental phenomena were observed.

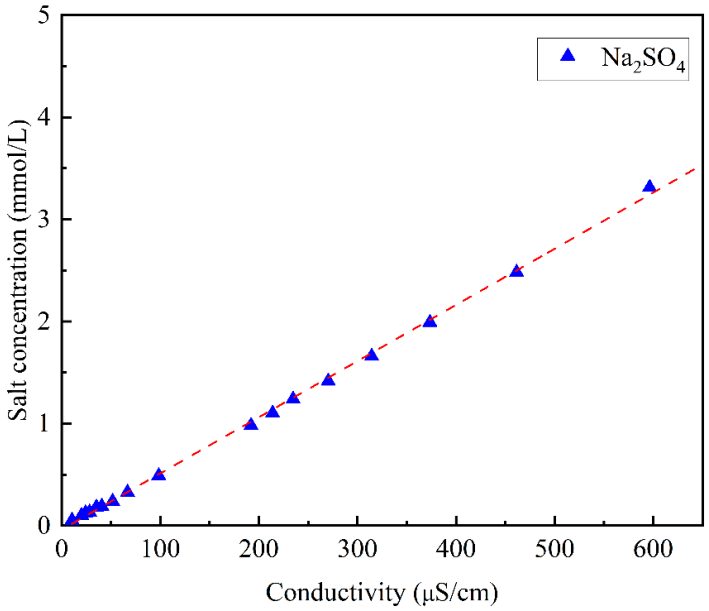

Figure 3. The concentration of Na_2SO_4 as a function of conductivity.

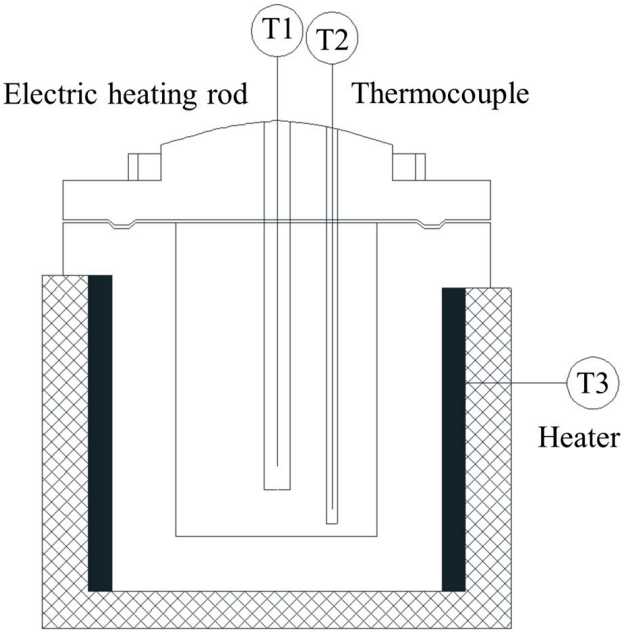

Figure 4. Schematic of high-pressure autoclave.

3. Model and Theory

In recent decades, various mathematical and numerical methods have been developed to study different supercritical fluid processes and analyze phenomena such as thermodynamics, hydrodynamics, crystal nucleation and growth, etc. These methods allow the prediction of nucleation times, temperature field distributions and supersaturation field distributions that are difficult to obtain experimentally. Computational fluid dynamics (CFD) software has been successfully applied to simulate flow, heat transfer and reactions under various supercritical conditions [28–31]. In a numerical simulation study of supercritical water desalination, Voisin et al. [32,33] used all the experimentally measured data as fitting parameters for numerical modeling and simulated the nucleation and growth of Na_2SO_4 particles under supercritical conditions, without considering crystal fragmentation and aggregation, and the simulation results were in good agreement with the experimental

data. Therefore, based on previous studies, CFD software was selected to simulate the temperature field inside the reactor to provide a better illustration of the effect of the heating rod on the temperature field inside the reactor and salt deposition.

3.1. Physical Model

The reactor comprises inlet piping, outlet piping, internal heating rods and an external heating furnace. To simplify the model, the flow paths inside the reactor were modeled, and the heating rod was approximated to the inner wall surface. Similarly, the external heating furnace was simplified to the outer wall's surface. Figure 5a,b shows the simplified physical model and the mesh of the model after meshing, respectively. The total number of cells was 872,842 and the specific information is summarized in Table 2 below.

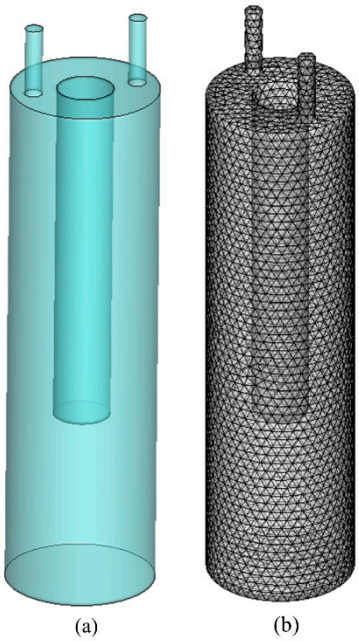

Figure 5. Physical model (**a**) and mesh for the modeling (**b**).

Table 2. Information for the mesh.

Cells	Faces	Nodes	Partitions
872,842	1,798,513	184,791	12 cell zones, 9 face zones

3.2. Grid Sensitivity Test

The grid sensitivity test was performed at a brine flow rate of 10 mL/min and an inlet temperature of 350 °C, under the heating rod surface temperature of 600 °C. Five grid sizes were compared: 5 mm, 3 mm, 1.5 mm, 1 mm, and 0.5 mm.

From the simulation results (Figure 6), it can be seen that the grid size of 0.5 mm did not improve the accuracy over that of 1 mm, so the grid size of 1 mm was used in the simulation.

3.3. Fluid Dynamics

Numerical calculations were carried out using the commercial software ANSYS FLUENT. Under the conditions studied in this work, the pressure was above the critical pressure. To simplify the calculation, it was assumed that the water at the entrance vaporized instantaneously. The vaporization was too fast to absorb heat from the surrounding environment, it would lead to the cooling of itself to provide heat of vaporization, while converting itself into water vapor. Furthermore, it was assumed that the average temperature of the

autoclave was 390 °C, and the state of water at the entrance (350 °C; 22.9 MPa) was liquid with the enthalpy of 1632 kJ/kg.

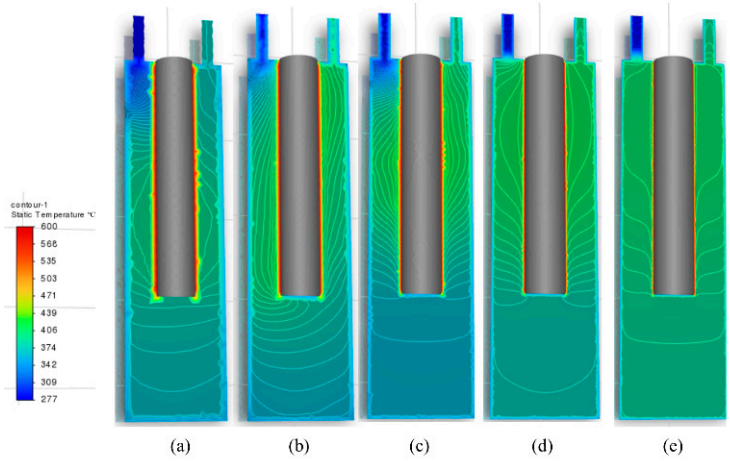

Figure 6. Grid sensitivity test. Grid size: (**a**) 5 mm, (**b**) 3 mm, (**c**) 1.5 mm, (**d**) 1 mm, and (**e**) 0.5 mm.

The inlet flow rates were set at 10, 20 and 50 mL/min, with an inlet temperature of 350 °C. The temperature of the heating rod was set at 600 °C and 900 °C, while the autoclave wall temperature was set at 350 °C. An implicit pressure-based solver was selected for the calculation and the coupling method of pressure and velocity was calculated using the SIMPLE algorithm. The residual convergence value was set at 10^{-3}.

The continuity equation is defined as follows:

$$\frac{\partial \rho}{\partial t} + \nabla \left(\rho \vec{v} \right) = 0 \tag{2}$$

For turbulence modeling, the standard k-ε model with standard wall functions is used as a near-wall treatment. In this model, the turbulent kinetic energy, k, and its dissipation rate, ε, are obtained from the following transport equations:

$$\frac{\partial}{\partial t}(\rho k) + \frac{\partial}{\partial x_i}(\rho k u_i) = \frac{\partial}{\partial x_j}\left[\left(\mu + \frac{\mu_t}{\sigma_k} \right) \frac{\partial k}{\partial x_j} \right] + G_k + G_b - \rho\varepsilon - Y_M \tag{3}$$

$$\frac{\partial}{\partial t}(\rho \varepsilon) + \frac{\partial}{\partial x_i}(\rho \varepsilon u_i) = \frac{\partial}{\partial x_j}\left[\left(\mu + \frac{\mu_t}{\sigma_\varepsilon} \right) \frac{\partial \varepsilon}{\partial x_j} \right] + c_{\varepsilon 1} \frac{\varepsilon}{k}(G_k + c_{\varepsilon 3} G_b) - c_{\varepsilon 2} \rho \frac{\varepsilon^2}{k} \tag{4}$$

where G_k denotes the turbulent kinetic energy due to the mean velocity gradient, G_b represents the turbulent kinetic energy due to buoyancy, and Y_M represents the effect of fluctuating expansion in compressible turbulence on the turbulent kinetic energy. $c_{\varepsilon 1}$, $c_{\varepsilon 2}$ and $c_{\varepsilon 3}$ are constants with values of 1.44, 1.92 and 0.09, respectively; σ_k and σ_ε are Prandtl numbers with values of 1.0 and 1.3, respectively.

The energy balance (equation) was used to consider the effect of heat transfer on fluid dynamics.

$$\frac{\partial}{\partial t}(\rho E) + \nabla \left(\vec{v}(\rho E + p) \right) = \nabla \left(k_{eff} \nabla T - \sum_j h_j \vec{J}_j + \left(\overline{\overline{\tau}}_{eff} \vec{v} \right) \right) \tag{5}$$

where k_{eff} is the effective thermal conductivity and $\vec{J}_j$ is the diffusive flux of the substance. The terms on the right-hand side indicate the energy transfer, diffusion and viscous dissipation caused by the conducting substance.

4. Results and Discussion

4.1. Solubility Data for Na_2SO_4

The solubility data for Na_2SO_4 in water at 380–420 °C and 23–25 MPa are shown in Table 3. The solubility range is 0.04–15.34 mmol/kg. The relationship between the experimental solubility data and temperature/pressure is illustrated in Figure 5.

Table 3. Solubility data for Na_2SO_4 at various temperatures and pressures.

P/MPa	T/°C	Solubility of Na_2SO_4 (mmol/L)
23	380	0.18
	390	0.07
	400	0.06
	410	0.05
	420	0.04
24	380	1.02
	390	0.45
	400	0.35
	410	0.32
	420	0.26
25	380	15.34
	390	1.58
	400	1.00
	410	0.44
	420	0.33

The solubility of Na_2SO_4 in supercritical water gradually decreases with increasing temperature and decreasing pressure. As shown in Figure 7, the solubility of Na_2SO_4 under supercritical conditions is strongly influenced by temperature and decreases significantly with increasing temperature, but its decreasing trend slows down when the temperature reaches 410 °C. After the temperature reached 390 °C, the solubility value was less than 2 mmol/L at any pressure (23–25 MPa). The effect of pressure on the solubility is more significant in the low-temperature zone, where the value falls with decreasing pressure. The influence of temperature and pressure on the solubility of salt is essentially an effect of the density of water. Thus, only in the lower temperature range, when the pressure has a greater impact on the density of water, will there be a significant change in the solubility of salt. After a temperature increase to a certain point, the water enters the low-density zone again, at which point the impact of pressure on solubility is no longer apparent.

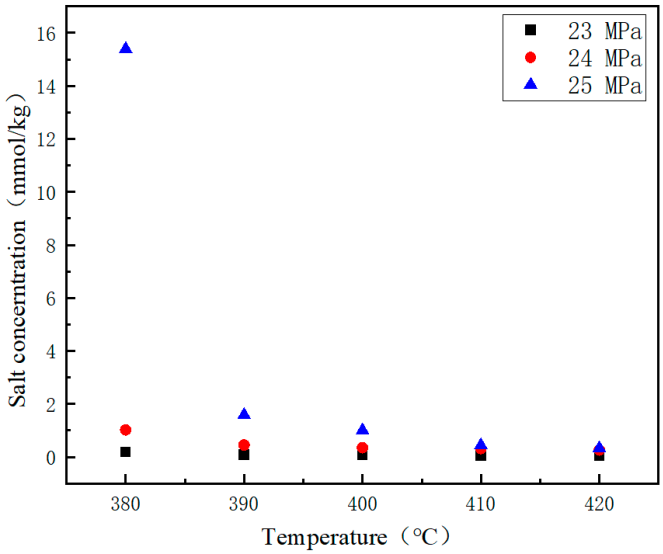

Figure 7. Solubility of Na_2SO_4 at different temperatures and pressures.

4.2. Results of Na_2SO_4 Salt Deposition Experiments

The experiments on salt deposition were conducted mainly at 390 °C due to the extremely low solubility of Na_2SO_4 under supercritical conditions (removal rate up to 90%). Table 4 lists a series of experimental information showing that there was no nickel foam on the heating rod and the bottom of the autoclave. The experiments of salt deposition with different heating rod temperatures and amounts of solution were conducted. The experimental results show that the superheated surface had a greater effect on the deposition form of Na_2SO_4, and loose salt particles could be seen on the heating rod and the bottom of the kettle (Figure 8a,b). The condition of the kettle bottom after the removal of the loose salt is shown in Figure 8c,f,i. It can be observed that at low heater rod temperatures, a thick compact layer of salt developed at the bottom of the kettle and that this layer had high mechanical strength making it difficult to remove, seriously affecting heat transfer efficiency and blocking. A comparison in Figure 8a,d indicates that when the heating rod temperature is higher, the kettle deposits more of the loosely shaped salt rather than the dense salt layer shown in Figure 8b, which is undoubtedly more beneficial for industrial operations.

Table 4. Experimental information of Na_2SO_4 with no materials.

Run	P/MPa	T1 [a]/°C	T2 [b]/°C	T3 [c]/°C	Amount of Solution/L
1	22.9	390	500	655–736	1.0
2	22.9	390	600	622.3–710.3	0.5
3	22.9	390	600	628.1–695.1	1.0

[a] T1 is the temperature in the kettle during the experiment. [b] T2 is the temperature of the heating rod. [c] T3 is the temperature of the heating furnace.

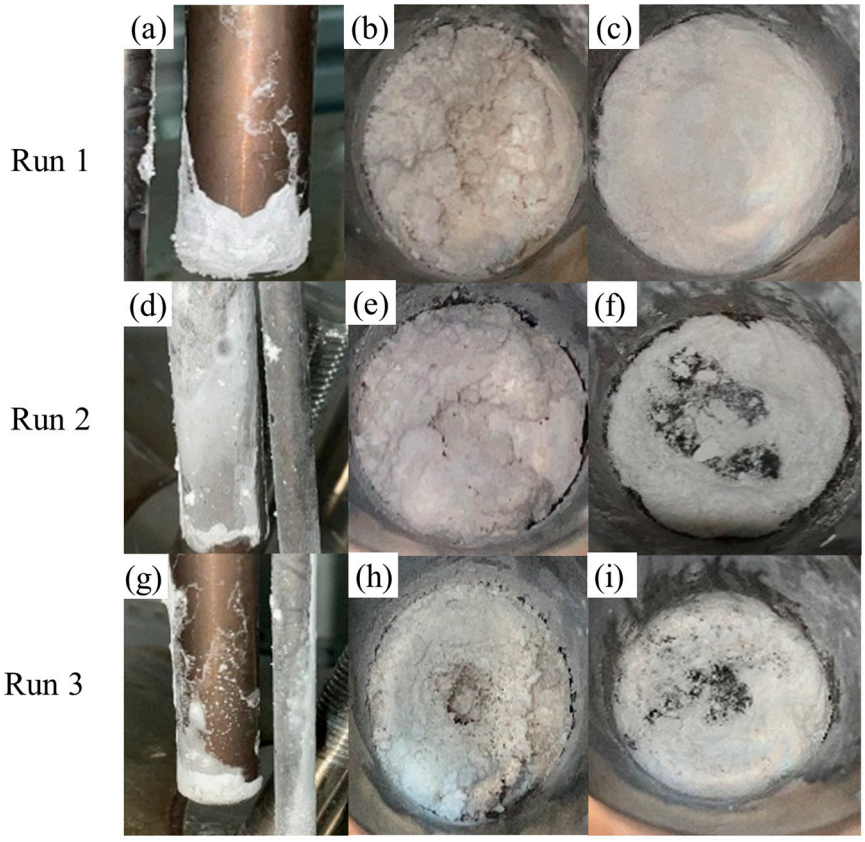

Figure 8. Deposition results of Na_2SO_4 without materials. Heating rod (**a**,**d**,**g**). Bottom of the reactor (**b**,**e**,**h**). Results affter removing the material and salt (**c**,**f**,**i**).

As shown in Figure 8d, a dense salt layer is more likely to form on the heating rod when the amount of solution is low. This is probably due to the fact that when the salt

concentration entering the reactor is low, the salt particles tend to nucleate on the heating rod. At this point, the nucleation rate is much higher than the growth rate, resulting in the formation of a salt film that covers the heating rod. However, the nucleation sites on the heating rod are covered as the solution is continuously introduced. Additionally, salt particles grow in aggregates on the formed salt nuclei, which are deposited at the bottom after being continuously detached by gravity, thus forming a loose salt lump.

To further verify the effect of nickel foam on salt deposition on the heating rod and at the bottom of the autoclave, several sets of experiments were conducted by varying the amount of brine passed (Table 5). When no material was placed on the heating rods, salt also appeared on the heating rods but did not accumulate as much as it did when the material was available (Figure 8g). The salt was mainly concentrated in the bottom space of the kettle. After arranging the nickel foam, it was evident that the salt was deposited preferentially on top of the nickel foam. When the nickel foam was set up close to the bottom wall, the deposited particles covered the material, in contrast to the case in the absence of material, when the dense salt layer disappeared close to the wall. The presence of nickel foam effectively inhibited the formation of a dense salt layer on the bottom of the autoclave. As the amount of solution passing through increases, the morphology of the salt deposited on the bottom tends to be more and more loose.

Table 5. Experimental information of Na_2SO_4 with materials on the heating rod and bottom of the kettle.

Run	P/MPa	T1 [a]/°C	T2 [b]/°C	T3 [c]/°C	Amount of Solution/L
1	22.9	390	600	608–690	0.5
2	22.9	390	600	637.8–673	0.75
3	22.9	390	600	627.7–706.8	1.0

[a] T1 is the temperature in the kettle during the experiment. [b] T2 is the temperature of the heating rod. [c] T3 is the temperature of the heating furnace.

It is noteworthy that the salt deposited on the material on the heating rod was primarily concentrated on the feed side, with salt particles also appearing on the reactor wall in the opposite position. Comparing the results on the heating rods (Figures 8g and 9g), it is evident that nickel foam effectively enhanced the induced crystallization of Na_2SO_4 on the heating rods.

4.3. Numerical Simulation Results

In order to better visualize the velocity distribution in the autoclave, the velocity field at different flow rates was simulated under a heating rod temperature of 600 °C and 900 °C. Figures 10 and 11 show the velocity field and the streamlines at different flow rates, respectively under a heating rod temperature of 600 °C, while the velocity field and the streamlines at different flow rates under a heating rod temperature of 900 °C are shown in Figures 12 and 13, respectively. At the three flow rates, the velocity in the autoclave tended to decrease gradually from the inlet to the inside of the kettle and formed a low-velocity zone in most of the area between the bottom of the heating rod and the bottom of the autoclave.

Figures 14 and 15 shows the temperature distribution at different flow rates when the heating rod temperature was 600 °C and 900 °C. It can be seen that despite the overall similarity in temperature distribution across the three flow rates, the temperature in proximity to the heating rod wall was significantly higher. Additionally, the region of the highest temperature within the autoclave was predominantly situated in the middle area of the heating rod. This phenomenon may explain the initial deposition of inorganic salts at the inlet following the placement of nickel foam on the heating rod. Considering the influence of temperature on the precipitation of inorganic salts under supercritical conditions, the heating rod surface serves as a preferential site for inorganic salt nucleation and precipitation, with sodium sulfate undergoing heterogeneous nucleation on the heating

rod. At the same time, due to the phase characteristics of sodium sulfate, after nucleation, it continues to grow and agglomerate and deposits at the bottom of the autoclave under the effect of gravity. This accounts for our observation of loosely packed large particle salt blocks at the bottom of the autoclave.

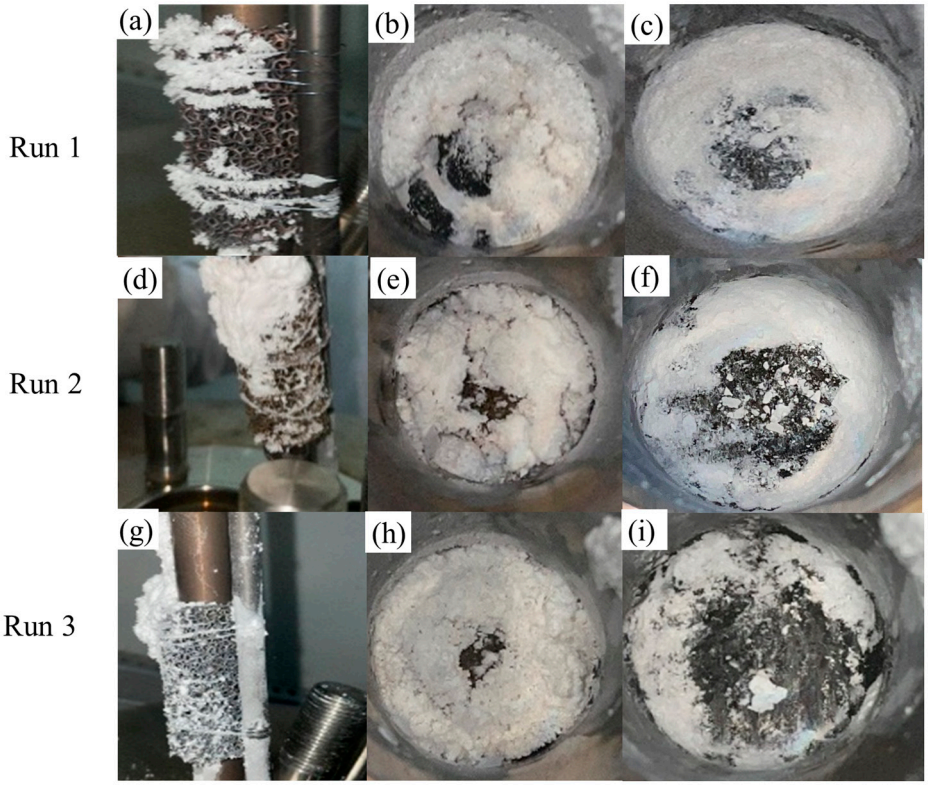

Figure 9. Deposition results of Na_2SO_4 with materials on the heating rod and bottom of the kettle. Heating rod: (**a**,**d**,**g**). Bottom of the reactor: (**b**,**e**,**h**). After removing the material and salt: (**c**,**f**,**i**).

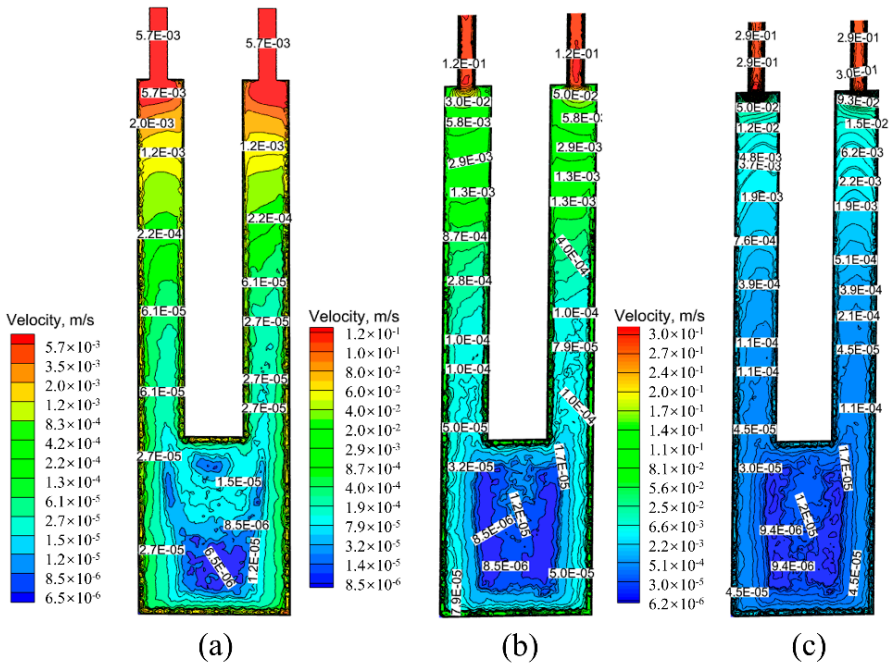

Figure 10. The contour of velocity in the reactor at different brine flow rates under a heating rod temperature of 600 °C: (**a**) 10 mL/min, (**b**) 20 mL/min, and (**c**) 50 mL/min.

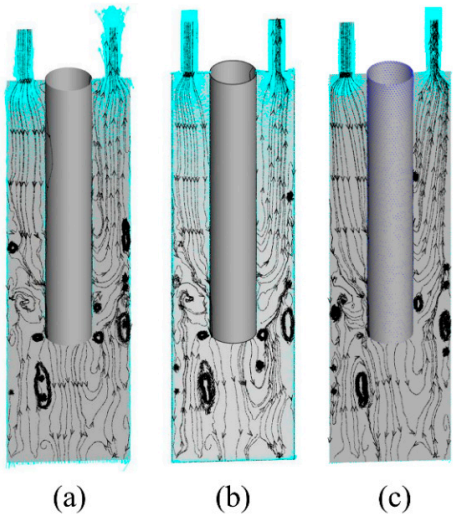

Figure 11. The streamlines in the reactor under a heating rod temperature of 600 °C at different brine flow rates: (**a**) 10 mL/min, (**b**) 20 mL/min, and (**c**) 50 mL/min.

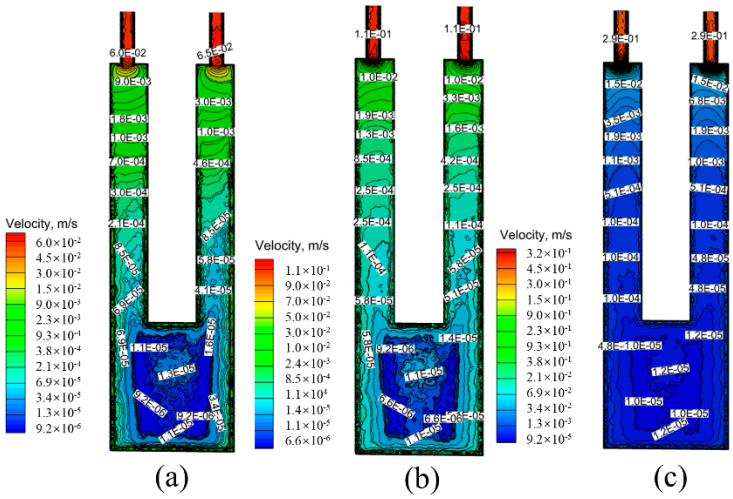

Figure 12. The contour of velocity in the reactor at different brine flow rates under a heating rod temperature of 900 °C: (**a**) 10 mL/min, (**b**) 20 mL/min, and (**c**) 50 mL/min.

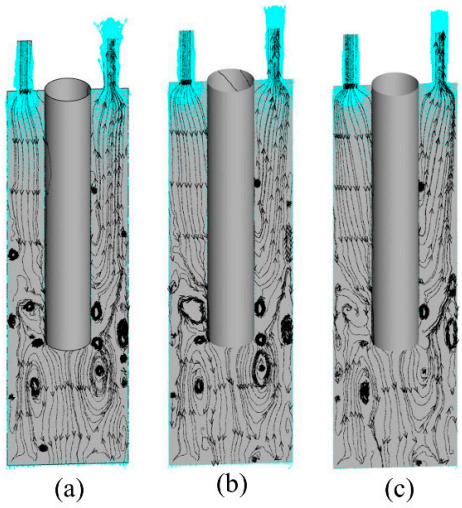

Figure 13. The streamlines in the reactor under a heating rod temperature of 900 °C at different brine flow rates: (**a**) 10 mL/min, (**b**) 20 mL/min, and (**c**) 50 mL/min.

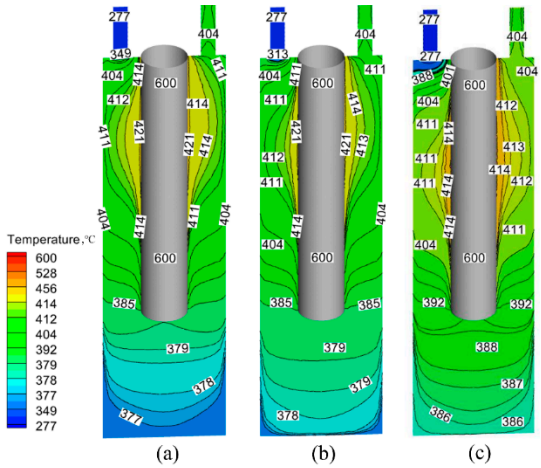

Figure 14. Temperature distribution at 600 °C of heating rod surface under different brine flow rates: (**a**) 10 mL/min, (**b**) 20 mL/min, and (**c**) 50 mL/min.

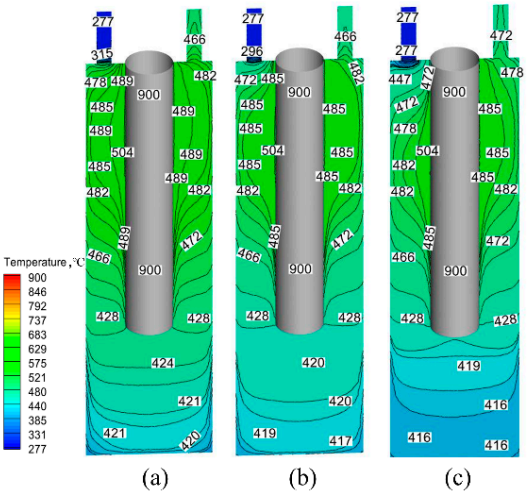

Figure 15. Temperature distribution at 900 °C of heating rod surface under different brine flow rates: (**a**) 10 mL/min, (**b**) 20 mL/min, and (**c**) 50 mL/min.

4.4. Analysis of the Mechanism of Salt Deposition

The nucleation mechanisms of crystals can be classified into two categories: homogeneous and non-homogeneous. Homogeneous nucleation occurs in the main fluid, while non-homogeneous nucleation occurs mainly on various surfaces. When the concentration of the brine in the autoclave is higher than the solubility under supercritical conditions, spontaneous homogeneous nucleation occurs in the solution [21]. The primary cause of salt precipitation is the significant alteration in the properties of the solvent water near the critical point. At the same time, the higher the temperature, the greater the supersaturation of the salt solution, and the faster the rate of salt crystallization and nucleation. As the autoclave is mainly heated by an external heater, the temperature of the wall is much higher than that of the fluid. Therefore, a large temperature gradient is formed near the walls, making the properties of the fluid preferentially change near the hot surface. The hot surface itself can also provide more adsorption sites for salt ions, resulting in a greater tendency for salt to nucleate on the high-temperature surface in non-homogeneous nucleation.

Figure 16b shows the binary phase diagram of Na_2SO_4 under a pressure of 25 MPa. Voisin [34] showed that aqueous Na_2SO_4 solution has a phase change under supercritical conditions. With an increase in temperature and concentration, Na_2SO_4 can precipitate readily as a solid phase (Figure 16b), instead of forming a gas–liquid coexistence state as it does in aqueous sodium chloride solutions (V + L region in Figure 16a). Thus, Na_2SO_4, as

a type II salt, is anticipated to preferentially crystallize in the region where supersaturated concentrations and high temperatures exist. Thereafter, rapid growth and aggregation are driven by concentration gradients and settling at the bottom is driven by gravity (Figure 17).

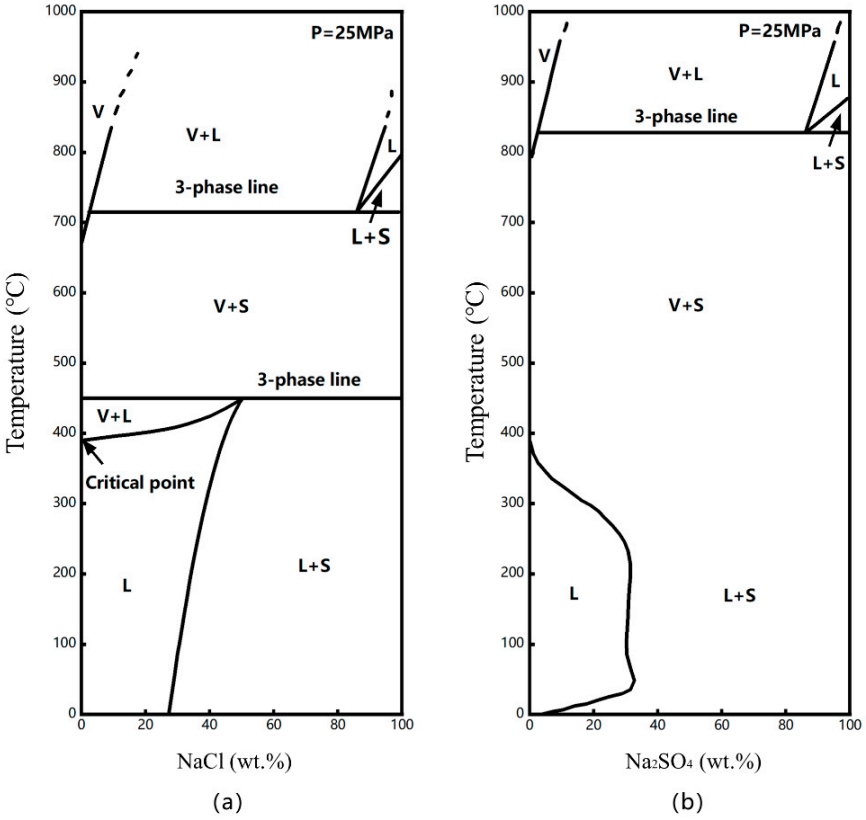

Figure 16. Temperature–concentration projections of phase diagrams at 25 MPa. (**a**) NaCl-H_2O and (**b**) Na_2SO_4-H_2O. L = liquid, V = vapor, S = solid (reconstructed from [35], copyright© (2004) Elsevier).

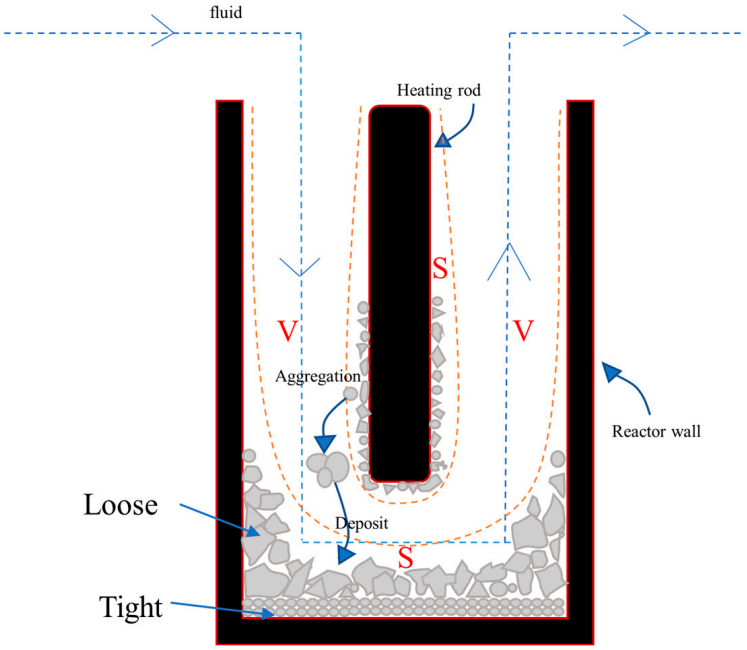

Figure 17. Schematic diagram of salt deposition mechanism in autoclave.

Foam metal exhibits better thermal conductivity than inorganic porous materials such as molecular sieves do due to its metallic nature. Direct contact with the superheated wall surface can extend the range of high-temperature regions near the wall. It can also provide a larger surface area, which facilitates the heterogeneous nucleation of Na_2SO_4. Due to the characteristics of its porous medium, Na_2SO_4 crystals have limited space to grow in it, making it difficult for the crystals to grow stably in a single direction. This may explain its effectiveness at inhibiting the formation of compact salt layers at the bottom of the autoclave (Figure 18).

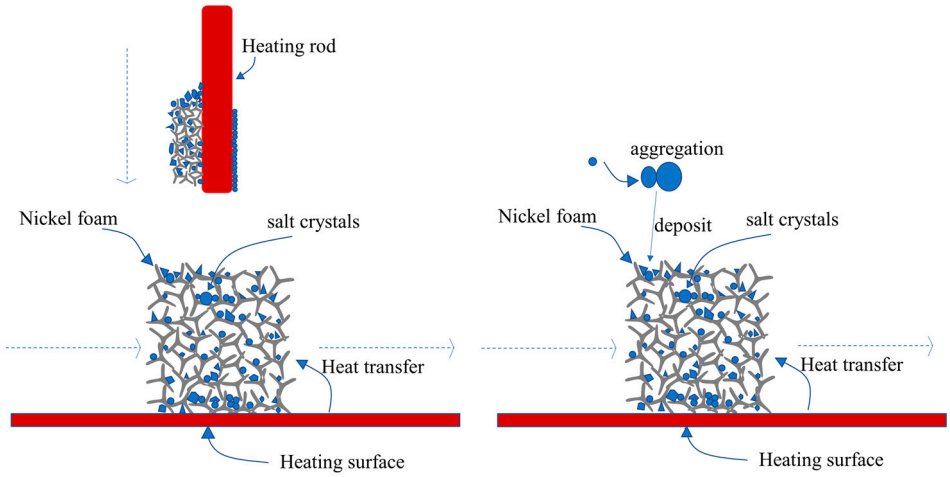

Figure 18. Schematic diagram of the effect of nickel foam on Na_2SO_4 salt deposition.

5. Conclusions

In this study, solubility data for Na_2SO_4 were initially obtained at 23–25 MPa and 380–420 °C. The removal rate of Na_2SO_4 from brine can reach more than 90% under supercritical conditions. Subsequently, a continuous apparatus with a heating rod was utilized to investigate the deposition characteristics of Na_2SO_4 in an autoclave at 23 MPa and 390 °C. The effect of superheated surfaces on the preferential nucleation growth of salt under supercritical conditions was examined. The findings indicated that Na_2SO_4 was deposited on the surface of the heating rod as well as on the bottom of the autoclave. This is related to the phase behavior of the salt; under supercritical conditions, the Na_2SO_4 separated into a gas phase and a solid phase, which was preferentially nucleated by the heater bar and grew along the inlet on it before being deposited due to the effect of gravity. Simulations using CFD software were conducted to obtain the temperature distribution in the reactor. The results showed that the temperature near the heating rod wall was higher than that of the main fluid, which was where the inorganic salts preferentially nucleated under supercritical conditions.

In addition, nickel foam was utilized as a porous medium to provide a large surface area for the superheated surface. As a carrier, it could accumulate significant amounts of salt on the heating rod, altering the state of the compact salt layer on the bottom of the autoclave. This presents a novel approach for the industrial recovery of inorganic salts under supercritical conditions.

However, hypersaline wastewater typically contains more than just Na_2SO_4, and for the supercritical water oxidation process, there is the oxidative transformation of organic matter as well. Therefore, it is crucial to investigate the phase behavior of other types of inorganic salts, the deposition phenomena, and whether or not the oxidation process of organic matter affects the deposition of inorganic salts in future work.

Author Contributions: Conceptualization, Z.C.; methodology, Z.L. and Q.Z.; investigation, Q.Z., Z.L. and Y.S.; supervision, Y.T., T.Y. and Z.C.; data curation, Q.Z. and Z.L.; writing—original draft preparation, Q.Z.; writing—review and editing, Q.Z. and Z.C. All authors have read and agreed to the published version of the manuscript.

Funding: This research received no external funding.

Data Availability Statement: All data collected in this study are contained within the article.

Conflicts of Interest: The authors declare no conflict of interest.

References

1. Leusbrock, I.; Metz, S.J.; Rexwinkel, G.; Versteeg, G.F. Quantitative approaches for the description of solubilities of inorganic compounds in near-critical and supercritical water. *J. Supercrit. Fluids* **2008**, *47*, 117–127. [CrossRef]
2. Deguchi, S.; Tsujii, K. Supercritical water: A fascinating medium for soft matter. *Soft Matter* **2007**, *3*, 797–803. [CrossRef] [PubMed]
3. Marrone, P.A. Supercritical water oxidation—Current status of full-scale commercial activity for waste destruction. *J. Supercrit. Fluids* **2013**, *79*, 283–288. [CrossRef]
4. Schmieder, H.; Abeln, J. Supercritical Water Oxidation: State of the Art. *Chem. Eng. Technol.* **1999**, *22*, 903–908. [CrossRef]
5. Marrone, P.A.; Hodes, M.; Smith, K.A.; Tester, J.W. Salt precipitation and scale control in supercritical water oxidation—Part B: Commercial/full-scale applications. *J. Supercrit. Fluids* **2004**, *29*, 289–312. [CrossRef]
6. Koda, S. Oxidation reactions of solid carbonaceous and resinous substances in supercritical water. *J. Supercrit. Fluids* **2009**, *47*, 400–406. [CrossRef]
7. Loppinet-Serani, A.; Aymonier, C.; Cansell, F. Supercritical water for environmental technologies. *J. Chem. Technol. Biotechnol.* **2010**, *85*, 583–589. [CrossRef]
8. Odu, S.O.; van der Ham, A.G.J.; Metz, S.; Kersten, S.R.A. Design of a Process for Supercritical Water Desalination with Zero Liquid Discharge. *Ind. Eng. Chem. Res.* **2015**, *54*, 5527–5535. [CrossRef]
9. van Wyk, S.; van der Ham, A.G.J.; Kersten, S.R.A. Analysis of the energy consumption of supercritical water desalination (SCWD). *Desalination* **2020**, *474*, 114189. [CrossRef]
10. van Wyk, S.; van der Ham, A.G.J.; Kersten, S.R.A. Potential of supercritical water desalination (SCWD) as zero liquid discharge (ZLD) technology. *Desalination* **2020**, *495*, 114593. [CrossRef]
11. Feng, W.; van der Kooi, H.J.; de Swaan Arons, J. Biomass conversions in subcritical and supercritical water: Driving force, phase equilibria, and thermodynamic analysis. *Chem. Eng. Process. Process Intensif.* **2004**, *43*, 1459–1467. [CrossRef]
12. Abdpour, S.; Santos, R.M. Recent advances in heterogeneous catalysis for supercritical water oxidation/gasification processes: Insight into catalyst development. *Process Saf. Environ. Prot.* **2021**, *149*, 169–184. [CrossRef]
13. Matsumura, Y.; Minowa, T.; Potic, B.; Kersten, S.; Prins, W.; Vanswaaij, W.; Vandebeld, B.; Elliott, D.; Neuenschwander, G.; Kruse, A. Biomass gasification in near- and super-critical water: Status and prospects. *Biomass Bioenergy* **2005**, *29*, 269–292. [CrossRef]
14. Hayashi, H.; Hakuta, Y. Hydrothermal Synthesis of Metal Oxide Nanoparticles in Supercritical Water. *Materials* **2010**, *3*, 3794–3817. [CrossRef]
15. Ye, N.; Yan, T.; Jiang, Z.; Wu, W.; Fang, T. A review: Conventional and supercritical hydro/solvothermal synthesis of ultrafine particles as cathode in lithium battery. *Ceram Int.* **2018**, *44*, 4521–4537. [CrossRef]
16. Yoko, A.; Seong, G.; Tomai, T.; Adschiri, T. Continuous Flow Synthesis of Nanoparticles Using Supercritical Water: Process Design, Surface Control, and Nanohybrid Materials. *Kona Powder Part J.* **2020**, *37*, 28–41. [CrossRef]
17. Pietrzak, K.; Krstulovic, N.; Blazeka, D.; Car, J.; Malinowski, S.; Wardak, C. Metal oxide nanoparticles as solid contact in ion-selective electrodes sensitive to potassium ions. *Talanta* **2022**, *243*, 123335. [CrossRef]
18. Amy, G.; Ghaffour, N.; Li, Z.Y.; Francis, L.; Linares, R.V.; Missimer, T.; Lattemann, S. Membrane-based seawater desalination: Present and future prospects. *Desalination* **2017**, *401*, 16–21. [CrossRef]
19. Lefebvre, O.; Moletta, R. Treatment of organic pollution in industrial saline wastewater: A literature review. *Water Res.* **2006**, *40*, 3671–3682. [CrossRef]
20. Goh, P.S.; Zulhairun, A.K.; Ismail, A.F.; Hilal, N. Contemporary antibiofouling modifications of reverse osmosis desalination membrane: A review. *Desalination* **2019**, *468*, 114072. [CrossRef]
21. Zhang, Y.; Wang, S.; Li, Y.; Zhang, J.; Xu, D.; Yang, C.; Yang, J.; Li, J.; Xu, T. Inorganic salts in sub-/supercritical water—Part A: Behavior characteristics and mechanisms. *Desalination* **2020**, *496*, 114674. [CrossRef]
22. Leusbrock, I.; Metz, S.; Rexwinkel, G.; Versteeg, G. Solubility of 1:1 Alkali Nitrates and Chlorides in Near-Critical and Supercritical Water. *Chem. Eng.* **2009**, *54*, 3215–3223. [CrossRef]
23. Rogak, S.N.; Teshima, P. Deposition of sodium sulfate in a heated flow of supercritical water. *AIChE J.* **1999**, *45*, 240–247. [CrossRef]
24. Yang, J.; Wang, S.; Li, Y.; Tang, X.; Wang, Y.; Xu, D.; Guo, Y. Effect of salt deposit on corrosion behavior of Ni-based alloys and stainless steels in supercritical water. *J. Supercrit. Fluids* **2019**, *152*, 104570. [CrossRef]
25. Xu, D.; Huang, C.; Wang, S.; Lin, G.; Guo, Y. Salt deposition problems in supercritical water oxidation. *Chem. Eng. J.* **2015**, *279*, 1010–1022. [CrossRef]

26. Dell'Orco, P.; Eaton, H.; Reynolds, T.; Buelow, S. The solubility of 1:1 nitrate electrolytes in supercritical water. *J. Supercrit. Fluids* **1995**, *8*, 217–227. [CrossRef]
27. Yang, J.Q.; Wang, S.Z.; Li, Y.H.; Xu, D.H. Under-deposit corrosion of Ni-based alloy 825 and Fe-Ni based alloy 800 in supercritical water oxidation environment. *Corros. Sci.* **2020**, *167*, 108493. [CrossRef]
28. Li, W.G.; Yu, Z.B.; Wang, Y.; Li, Y.L. Heat transfer of supercritical carbon dioxide in a tube-in-tube heat exchanger-a CFD study. *J. Supercrit. Fluid.* **2022**, *181*, 105493. [CrossRef]
29. Demoisson, F.; Ariane, M.; Leybros, A.; Muhr, H.; Bernard, F. Design of a reactor operating in supercritical water conditions using CFD simulations. Examples of synthesized nanomaterials. *J. Supercrit. Fluid.* **2011**, *58*, 371–377. [CrossRef]
30. Nadimpalli, N.K.V.; Bandyopadhyaya, R.; Runkana, V. A coupled CFD-PBM and thermodynamic analysis of continuous supercritical hydrothermal synthesis of nanoparticles. *J. Supercrit. Fluid.* **2018**, *136*, 164–179. [CrossRef]
31. Leybros, A.; Piolet, R.; Ariane, M.; Muhr, H.; Bernard, F.; Demoisson, F. CFD simulation of ZnO nanoparticle precipitation in a supercritical water synthesis reactor. *J. Supercrit. Fluid.* **2012**, *70*, 17–26. [CrossRef]
32. Voisin, T.; Erriguible, A.; Philippot, G.; Ballenghien, D.; Mateos, D.; Cansell, F.; Iversen, B.B.; Aymonier, C. Investigation of the precipitation of Na2SO4 in supercritical water. *Chem. Eng. Sci.* **2017**, *174*, 268–276. [CrossRef]
33. Voisin, T.; Erriguible, A.; Aubert, G.; Aymonier, C. Aggregation of Na_2SO_4 Nanocrystals in Supercritical Water. *Ind. Eng. Chem. Res.* **2018**, *57*, 2376–2384. [CrossRef]
34. Voisin, T.; Erriguible, A.; Aymonier, C. Influence of multiphasic systems on salt(s) solubility in supercritical water: The case of NaCl and NaCl-Na_2SO_4. *J. Supercrit. Fluids* **2019**, *152*, 104567. [CrossRef]
35. Hodes, M.; Marrone, P.A.; Hong, G.T.; Smith, K.A.; Tester, J.W. Salt precipitation and scale control in supercritical water oxidation—Part A: Fundamentals and research. *J. Supercrit. Fluids* **2004**, *29*, 265–288. [CrossRef]